Highly Ductile Limits for Deep Steel Columns

Tung-Yu Wu, S.M.ASCE[1]; Sherif El-Tawil, Ph.D., P.E., F.ASCE[2]; and Jason P. McCormick, Ph.D., A.M.ASCE[3]

ABSTRACT

The collapse behavior of individual deep columns subjected to realistic loading and boundary conditions is investigated in this study. Loading protocols that are representative of seismic demands on first-story columns are developed through simulations of complete frames subjected to collapse-inducing seismic loading. A set of deep columns that cover a wide range of both global and local slenderness ratios representative of commercially available deep sections is used to investigate and codify the effects of three key parameters: level of axial loading, global slenderness (L/r_y) and web slenderness (h/t_w). Current design recommendations are critiqued and modified provisions that incorporate the influential parameters identified in this study are proposed for designing highly ductile members for seismic applications. The new provisions are proposed in a format that can facilitate adoption into future specifications.

INTRODUCTION

The use of deep, slender wide flange sections, with a depth of 600 mm (24 inches) or greater, has been prevalent in special moment frames (SMFs) since the late 1990s. The large depth, high in-plane flexural stiffness and strength make such sections an attractive choice for engineers seeking to satisfy current panel zone, drift and strong-column/weak-beam design

[1]Ph.D. Candidate, Department of Civil & Environmental Engineering, University of Michigan, Ann Arbor, MI 48109-2125; email: tungyuwu@umich.edu
[2]Professor, Department of Civil & Environmental Engineering, University of Michigan, Ann Arbor, MI 48109-2125; email: eltawil@umich.edu
[3]Associate Professor, Department of Civil & Environmental Engineering, University of Michigan, Ann Arbor, MI 48109-2125; email: jpmccorm@umich.edu

criteria. However, deep columns are also susceptible to weak-axis global and lateral torsional buckling, leading to potential vulnerabilities that are not yet fully understood (NIST 2011).

To address this shortcoming, NIST (2011) proposed a comprehensive analytical and experimental research plan to better understand the inelastic behavior of deep steel columns. The plan had three categories of proposed research needs: member, subassemblage, and system level studies. A number of researchers have conducted computational and experimental studies at the member (Fogarty and El-Tawil 2015, Elkady and Lignos 2015, Uang et al. 2015, and Elkady and Lignos 2016) and system levels (Wu et al. 2017), but not yet at the subassemblage level.

Using computational simulation, Fogarty and El-Tawil (2015) investigated the collapse resistance of steel columns under combined axial and lateral loading. They noted that many deep sections considered highly ductile per current provisions cannot reach a 4% drift ratio under feasible axial loads (0.2-0.4 P_y, where P_y is the axial yield strength of the column cross section). They also showed that while the flange slenderness ratio ($b_f/2t_f$, where b_f is flange width and t_f is flange thickness) has a minor effect on column collapse capacity when the current AISC highly ductile limit for flange slenderness is satisfied, web (h/t_w, where h is web height and t_w is web thickness) and global slenderness (L/r_y, where L is the unbraced column length and r_y is radius of gyration about the column's weak-axis) ratios are highly influential. They proposed equations that assessed the peak axial load capacity of the column as a function of these parameters.

Elkady and Lignos (2015) studied the cyclic behavior of deep columns through detailed finite element analyses. They noted that current seismic requirements for highly ductile sections were not adequate for interior columns subjected to an axial load of 0.2-0.35 P_y. Uang et al. (2015)

conducted experiments to study the cyclic behavior of deep column specimens under a symmetric cyclic drift loading combined with a constant axial load of 0.2-0.6 P_y. Most specimens were not able to deliver a plastic rotation of 0.03 radian without a reduction in maximum flexural strength of 10% or more during the test.

A common finding in the above studies is that the capacity of deep steel columns may be lower than expected by current seismic design specifications (AISC 2016a) for highly ductile members, especially when the axial load is larger than 0.20 P_y. However, the symmetric loading schemes as well as idealized boundary conditions employed in these studies do not fully reflect system-level demands. Wu et al. (2017) observed much better component performance in their system studies and suggested that system demands could be significantly milder than those used in studies of isolated columns. Elkady and Lignos (2016) also pointed out the significant difference in column capacity under different loading protocols.

The recent Wu et al. (2017) and Elkady and Lignos (2016) studies suggest that the inelastic behavior of deep columns is still not yet well understood. Moreover, while L/r_y was shown to be an influential variable in Fogarty and El-Tawil (2015), it is not considered in current AISC highly ductile member limits (AISC 2016a). With these shortcomings as motivation, this study is geared towards providing new, detailed insight into deep column behavior under realistic seismic demands. To this end, a frame system analysis is first performed to investigate the drift and force demands on first-story columns during feasible seismic collapse scenarios and to develop representative models for individual column analysis. Then, a set of deep columns that cover a wide range of both local and global slenderness ratios is used to identify and study key parameters affecting deep column behavior. The insight gained from these computational studies is used as a basis for critiquing current AISC design guidelines (AISC 2016a) and proposing improved provisions suitable for adoption into current specifications.

SYSTEM ANALYSIS

Earthquake-induced collapse simulations of a four-story frame are performed using ground motions selected from the far-field record set in FEMA P695 (2009). The results of the computational studies are used to develop meaningful and realistic loading protocols for first-story columns.

Prototype Building

The four-story building outlined in NIST (2010) is selected as the prototype building. The building's plan is shown in Fig. 1(a). The building has three-bay steel SMFs on each of its exterior sides, which are assumed to resist all the seismic demands on the building. The circled frame in Fig. 1(a), whose elevation is shown in Fig. 1(b), is considered for further study in this work. The frame is assumed to carry the tributary gravity loads indicated in Fig. 1(a). Member sizes in Fig. 1(b) and in the rest of the paper are listed in English units (in. x lb/ft) because this naming scheme is widely recognized. The SMFs are designed with deep columns and reduced beam sections (RBS) using ASTM A992 steel in accordance with AISC (2016a, 2016b) and ASCE (2010). The site class of the building is *D* and the seismic design category (SDC) is D_{max}. Further design details of the building can be found in NIST (2010).

Modeling Approach

Detailed finite element models of the SMF are created using Hypermesh (2013) and analyzed using LS-DYNA (2013). The building model is discretized using fully integrated shell elements (ELFORM 16) based on the formulation published by Engelmann et al. (1989). The meshing scheme employed by Fogarty and El-Tawil (2015) is used in this research, as shown in Fig. 2. A strain rate-independent, nonlinear, kinematic hardening material model (MAT_153) developed by Huang and Mahin (2010), is assigned to the shell elements. This material model has two back stress terms for kinematic hardening combined with linear isotropic hardening. In order to calibrate the hardening parameters, a true stress-true strain curve is constructed by incorporating the minimum mechanical properties of A992 steel with an expected material strength ratio of 1.1 in the model proposed by Arasaratnam et al. (2011). The calibration result is shown in Fig. 3.

The SMF is assumed fully fixed at its base. The lateral bracing of the SMF is simulated by preventing out-of-plane translation at key nodes (Fig. 2(b)). Both flanges of the beams are laterally braced at locations with a spacing L_b that satisfies the requirement for highly ductile members in AISC (2016a). Column flanges in the beam-column connection region are laterally braced at the levels of both beam flanges. System-wide P-Delta effects are considered by connecting a leaning column to the SMF with rigid truss members as shown in Fig. 2(a). A gravity load equal to half of the building floor mass minus that distributed to the SMF system is applied at each floor of the leaning column. A mass weighted damping of 2.5% is assumed at the first mode period (1.67 s) of the SMF.

The axial load induced by the tributary gravity load indicated in Fig. 1(a) is 0.14 P_y and 0.2 P_y for interior and exterior SMF columns, respectively, where P_y is the axial yield strength of the section based on an expected yield stress of 379 MPa. This case is designated TGL14. To promote vertical progressive collapse, another case is considered where the gravity load on the SMF is increased to a value that causes an axial load of 0.2 P_y and 0.3 P_y on the interior and exterior SMF columns, respectively. For this case (designated TGL20), the load on the leaning column is adjusted down to ensure that the total building mass remains the same.

Model Validation

The finite element models used in this work were thoroughly validated by Fogarty et al. (2017)

using cyclic experimental data from deep column specimens in Uang et al. (2015). The test matrix used in the validation studies included five W24 sections and three levels of axial load that resulted in a total of twenty-five specimens categorized into eight groups. The column specimens were 5.49 m long, tested with fixed-fixed boundary conditions, and subjected to a combination of a constant axial force and a symmetric cyclic drift loading associated with steel beam-to-column moment connection tests as outlined in AISC (2016a). The validation study showed that the finite element models were able to reasonably capture the shape, length, and occurrence of local and global buckling behavior. Additional details can be found in Fogarty et al. (2017), which in the interest of space, are not repeated here.

Development of Lateral Drift Protocol

Eleven ground motions are selected from the Far-Field record set in FEMA P695 (2009) and scaled up until they induce collapse of the SMF. For the TGL14 situation, nine of eleven ground motions induce sidesway collapse of the SMF as shown in Fig. 4(a). The corresponding first-story drift histories for the nine records are plotted in Fig. 5(a) and are used to develop a representative protocol for sidesway collapse. As seen in Fig. 5(a), the drift histories have initial cyclic response followed by ratcheting behavior, where the frame keeps leaning farther and farther until it collapses. A loading protocol that is deemed to reflect this behavior is shown as a solid dark line in Fig. 5(a). It starts with a group of symmetric cycles followed by generally increasing drift that incorporates three groups of ratcheting loading cycles. The symmetric group has six cycles with increasing magnitudes, while each ratcheting group consists of two small and one large reversed loading cycles. This protocol is designated CR (cyclic ratcheting) protocol.

In the TGL20 situation, the higher initial gravity load increases the possibility of vertical progressive collapse. Of the 11 applied histories, seven ground motions induce vertical progressive collapse of the SMF as they are scaled up. A typical collapse response is shown in Fig. 4(b). As with sidesway collapse, the drift histories also show initial symmetric cycles followed by ratcheting behavior. The main difference is that the drift does not increase as sharply as in TGL14. Collapse occurs at smaller drift levels, in the range of 2% to 6% rather than about 10% for TGL14, as shown in Fig. 5(b). The selected drift history deemed to represent the observed histories is shown as a solid dark line in Fig. 5(b). The selected protocol has the same number of cycles and reversed loadings as the CR protocol but with larger amplitudes. It is designated CR2.

The CR and CR2 protocols represent realistic drift demands imposed by a ground motion on a column in a collapsing structural system. These loading protocols are used, along with others, to investigate the inelastic behavior of axially loaded columns undergoing lateral drift.

ANALYSIS OF COMPONENT COLUMN MODELS

Conducting parametric simulations with the full SMF to study the collapse behavior of steel columns is computationally intractable. Therefore, component column models are used instead. To ensure that the component models yield results that are close to the system results, a series of parametric simulations are conducted to identify the most realistic boundary conditions and drift loading histories for the component model.

Component Model Setup

The column length is taken as 3.96 m, which is the same as the clear floor height of the prototype moment frames. Initial column imperfection is considered by applying a geometric perturbation with an out-of-plane sinusoidal shape. The maximum deflection of the imperfection at mid-height of columns is L/1000, which corresponds to the maximum out-of-straightness tolerance per AISC (2016c).

Interior columns do not see large variations in axial loading while exterior columns are subjected to significant fluctuations in the axial load level during seismic events. The axial loading on exterior column members increases greatly at higher drift levels as a result of the overturning moments on the system. To approximate these effects and enable practical treatment of the problem using component models, interior columns are assumed to carry a constant gravity load, P_g, during their entire drift history. Exterior columns are also assumed to carry a constant gravity load during their drift history, but are further compressed at peak drift to reflect the increase in load demands on exterior columns. The constant compressive axial load in both cases is $P_g = 0.2P_y$, which is the axial load threshold at which unsatisfactory column behavior starts to occur as noted in Fogarty and El-Tawil (2015), Elkady and Lignos (2015), and Uang et al. (2015).

The bottom end of the prototype column is assumed to be fully fixed. For the top end, three boundary conditions are explored, as shown in Fig. 6(a): (1) both in-plane and out-of-plane rotations are fixed (fixed-fixed, FF), (2) in-plane rotation is fixed, while out-of-plane rotation is allowed (fixed-pinned, FP), and (3) in-plane rotation is restrained by an elastoplastic spring with a flexural stiffness, yield moment and hardening post-yield response obtained from subassembly analysis, while out-of-plane rotation is fixed (spring-fixed, SF). The FF condition is similar to that used by Uang et al. (2015) in their experiments. The FP was used by Fogarty et al. (2017) in their computational studies, while the SF condition is newly used in this study to capture the nonlinear, partial rigidity of adjacent beam-column connections.

The subassembly used to determine the properties of the elastoplastic spring is taken from the frame at the inflection points of the beams and columns as shown in Fig. 6(b). A small push load is first applied at the tip of the second-story column to determine the flexural stiffness of the spring using the moment and rotation measured at the top end of the first-story column (see Fig. 6(b)). The push load is then increased until plastic hinges form in the beams. The corresponding moment at the column top end is taken as the yield moment of the spring. The flexural stiffness and yield moment obtained from the subassembly are obtained for interior columns that are W24x103. When other member sections are used, the values are linearly modified based on their flexural stiffness and plastic modulus, respectively. For exterior columns, the flexural stiffness and yield moment are halved to reflect the fact that only one beam is connected to the columns.

In addition to the CR and CR2 loading protocols, two other protocols are used, monotonic (designated M), and symmetric cyclic (designated SC). The former was used in the computational studies of Fogarty et al. (2017), while the latter was used in the experimental research by Uang et al. (2015). The four loading schemes used in this work are shown in Fig. 7, where the drift level is plotted versus time on the horizontal axis. The loading speeds (and hence times on the horizontal axis of Fig. 7) are selected through a trial and error process to be low enough so as not to excite unwarranted dynamic effects and yet fast enough to permit the simulations to be conducted in a timely manner.

Collapse is deemed to occur when a column is unable to sustain the applied axial load (explicit collapse) due to instability, i.e. the column unloads and the axial force in it drops suddenly (Fogarty and El-Tawil 2015). The maximum drift ratio (DR_{max}) achieved prior to axial failure is then recorded and taken as the drift capacity of the column.

In order to facilitate discussion of the research parameters, columns under specific loading schemes are designated as W-X-Y, where “W” is the section, “X” is the boundary condition, “Y” is the drift loading protocol. For example, W24x103-FP-CR is the W24x103 column with FP boundary conditions subjected to CR loading.

Effect of Boundary Conditions

Collapse simulations are conducted for a variety of component models with W24 sections. The results of the simulations indicate that the performance of FP columns is substantially worse than columns with other boundary conditions, as shown in Fig. 8(a), which plots DR_{max} versus section weight for various boundary conditions. The reason for the poorer performance under FP conditions is that FP columns are more sensitive to changes in the end restraints of the member, which are affected by accumulation of local buckling at the column ends as a result of large drift loading. The evolving local damage leads to stiffness and strength degradation of the effective boundary conditions at the column ends, essentially increasing the effective buckling length and hence lowering the axial strength of the column. At the other extreme, columns with SF conditions generally have the highest drift capacities. The improved performance stems from the flexibility of in-plane rotation at the top end of the columns, which reduces the demand at the top end and delays local buckling.

Effect of Loading Protocols

Fig. 8(b) shows the effects of loading protocol on the drift capacity of columns with FP boundary conditions. It shows that most of the columns subjected to M and CR loading can sustain the applied axial loads up to 10% drift ratio. While some light columns failed before reaching their end point of 4% drift under the CR2 protocol, e.g. DR_{max} of W24x84-FP-CR2 is 3.5%, several heavier columns survived without collapse to 4% drift under this protocol. However, unlike the other protocols, the SC protocol significantly decreases drift capacity. Indeed, most of the columns cannot reach 4% drift under the SC protocol. For example, DR_{max} of W24x84-FP-SC is only 1.5%.

The simulation results, including those in Fig. 8(b), show that the damage due to the SC protocol is more severe than that due to other schemes. The reasons for this can be better appreciated in Fig. 9, which shows the force versus drift performance and local buckling at 4% drift of the W24x103-SF column under different drift protocols. As marked by the red circles in Fig. 9, the column's lateral strength at 4% drift under the SC protocol is only 43% and 36% of that under the CR2 and M protocols, respectively. The explanation for these observations stems from the amount of local buckling in the plastic hinge regions associated with the various loading schemes, which can be seen in the buckled shapes that correspond to the marked circles. The SC protocol tends to cause substantial local buckling at the column ends (Fig. 9(c)), which reduces the end restraint and promotes global instability. M loading causes local buckling at only one side of the column end (compression side, see Fig. 9(d)), limiting the amount of degradation in the boundary restraints and allowing the columns to reach larger drifts than their SC counterparts. A similar phenomenon (compared to M loading) can also be observed at the ends of columns under the CR and CR2 protocols as shown in Fig. 9(a) and 9(b), respectively. The columns under the CR2 protocol experienced more severe local buckling on both sides of the column than under the CR protocol, providing explanation for why the CR2 protocol is more damaging than the CR one.

Comparison between Column and Frame Analysis

Fig. 10(a) shows the deformed shape of an interior W24x103 column at 4% drift in the four-story frame with TGL20 conditions. The frame is subjected to the Kobe/SHI000 record with S_a(1.67s, 5%)=0.36g and undergoes sidesway collapses. Fig. 10(b) through 10(d) show the response of individual columns at 4% drift for a variety of boundary and loading conditions, namely for W24x103-SF-CR, W24x103-FF-SC, and W24x103-FP-M, respectively. Clearly, the W24x103-SF-CR case (Fig. 10(b)) matches the column in Fig. 10(a) well and therefore has an appropriate combination of boundary and loading conditions for simulating an interior column in a sidesway collapse scenario.

Fig. 11(a) and 11(c) show the deformed shape of interior and exterior columns (both W24x103), respectively, at 4% drift in the four-story frame with TGL20 condition, undergoing vertical progressive collapse. The frame is subjected to the Northr/MUL009 with a S_a(1.67s, 5%) of 1.19g. The deformed shape of W24x103-SF-CR2 is shown in Fig. 11(b), which is reasonably consistent with the shape in Fig. 11(a). The same is true for the exterior column in Fig. 11(c) and its individual column comparison in Fig. 11(d). Although the failure shapes for the exterior column (compare Fig. 11(c) to Fig. 11(d)) do not relate as well as they do for interior columns, the squash strength of the individual column is 0.53 P_y, which is close to the maximum axial force of 0.49 P_y seen in the frame's exterior column during the earthquake.

Implications of Component Column Study

The computational results demonstrate that the SF boundary condition is the most realistic one among the various combinations considered. When applied to an individual column, both the CR and CR2 protocols reasonably represent the demands seen at the system level. In the remainder of the paper, SF boundary conditions are applied in conjunction with the CR2 protocol, which represents a severe design situation, to investigate the effect of section properties and develop proposed design guidelines.

PARAMETRIC STUDY OF SECTION PROPERTIES

A set of deep columns that cover a wide range of both global and local slenderness ratios are analyzed using component column models. The selected sections and their properties are listed in Table 1 and cover a broad range of slenderness parameters as shown in Fig. 12. The seismic slenderness limits specified in AISC (2016a) for highly ductile members (λ_{hd}) made of A992 steel (with an expected yield stress ratio R_y = 1.1) are also plotted. In AISC (2016a), a highly ductile member is defined as a member that is "intended to withstand significant plastic rotation of 0.04 rad or more during the design earthquake". The highly ductile limit (HDL) for flange slenderness ratio ($b_f/2t_f$) is

$$\lambda_{hd} = 0.32\sqrt{E / R_y F_y} \tag{1}$$

The highly ductile limit for web slenderness ratio (h/t_w) is

$$\lambda_{hd} = 2.57\sqrt{E / R_y F_y}(1 - 1.04C_a) \text{ for } C_a \leq 0.114 \tag{2}$$

$$\lambda_{hd} = 0.88\sqrt{E / R_y F_y}(2.68 - C_a) \geq 1.57\sqrt{E / R_y F_y} \text{ for } C_a > 0.114 \tag{3}$$

where $C_a = P_u/\phi_c P_y$, which is the ratio of required axial strength using LRFD combinations, P_u, to expected yield strength, $P_y = R_y F_y A_g$, multiplied by the resistance factor for compression, ϕ_c.

Because $b_f/2t_f$ has been shown to have a minor effect on column collapse capacity when it satisfies the current AISC highly ductile limit (Fogarty and El-Tawil 2015), all the selected sections have a $b_f/2t_f$ below this limit to investigate the more significant factors, h/t_w and L/r_y, as shown in Fig. 12. The prototype columns are created using the selected W24, W27, and W30 sections with base lengths of 3.96, 4.27, and 4.57 m, respectively. More analysis cases are created by increasing these lengths in order to cover a wide range of L/r_y resulting in a total of 65 column models. The slenderness properties of these columns as well as the highly ductile limits for h/t_w are shown in Fig. 12 (b). Because there is no highly ductile limit for L/r_y of columns in AISC (2016a), the limit for a column with an unbraced beam-to-column connection, which is 60, is plotted instead.

Performance Parameters

Two performance parameters are considered. The first one is the critical constant axial load ratio (CCALR). The critical constant axial load is defined as the maximum constant axial load ratio (P_g/P_y) that a column can sustain and still reach 4% drift under a prescribed protocol, as shown in Fig. 13(a). Due to a compromise between precision and computational cost, the CCALR is determined in 0.05 increments. As noted earlier, interior columns do not see large variations in their axial load demands during a seismic event, therefore CCALR is representative of the collapse capacity of an interior column in a SMF.

The second performance parameter is the post-drift strength ratio (PDSR). The PDSR is defined as the squash capacity of a column at 4% drift after being subjected to a prescribed drift protocol under a given constant axial load (Fig. 13(b)). The PDSR is the ratio of post-drift strength of the column to P_y and, per the earlier discussion of exterior column behavior, is considered to be an indicator of the collapse capacity of an exterior column in a SMF.

Influence of Key Variables on Column Behavior

The CCALRs and PDSRs of the prototype columns are shown in Table 1 as well as Fig. 14 and 15, respectively. Linear regression analysis is used to tie the CCALR and PDSR values to the web and global slenderness ratios and level of initial axial load. For CCALR, the significant parameters are h/t_w and L/r_y and the predictive function obtained from regression is:

$$\text{CCALR} = 0.72 - 0.0044\frac{h}{t_w} - 0.0027\frac{L}{r_y} \tag{4}$$

for deep columns with $b_f/2t_f$ satisfying current highly ductile limits (i.e. $0.32\sqrt{E/R_yF_y}$), 15 < h/t_w < 50, and 45 < L/r_y < 120. For PDSR, the significant parameters are h/t_w, L/r_y, and P_g/P_y and the predictive function is:

$$\text{PDSR} = 1.71 - 0.011\frac{h}{t_w} - 0.0055\frac{L}{r_y} - \frac{P_g}{P_y} \tag{5}$$

for deep columns with $b_f/2t_f$ satisfying current highly ductile limits, 15 < h/t_w < 50, 45 < L/r_y < 120, and 0.2 < P_g/P_y < 0.4. When applying Equation (5), P_g/P_y should be smaller than CCALR otherwise the column cannot support P_g/P_y up to 4% drift. To avoid computing CCALR for exterior columns, the values obtained from Equation (4) can be used instead even though they were developed for interior columns. CCALR values from Equation (4) are conservative because interior columns have larger in-plane rotational restraint at the top compared to exterior columns, which leads to lower column axial capacity and, hence, CCALR. The predictive functions are shown as a contour plot with the data in Fig. 14 and 15.

Fig. 14 shows that there is a strong inverse relationship between CCALR and both web and global slenderness ratios (h/t_w and L/r_y). For columns with L/r_y about 80, increasing h/t_w from 15 to 50 reduces CCALR from 0.45 to 0.25. For columns with h/t_w about 37, the CCALR decreases from 0.4 to 0.2 when L/r_y increases from 52 to 115. These results show that both h/t_w and L/r_y have a significant effect on the collapse capacity of deep columns.

For ϕ_c = 1.0, the current highly ductile limit per Equation 3 is plotted in Fig. 14 as a sloping dotted line. The line represents the intersection between Equations 3 and 4. In other words, the line represents the condition $P_g = P_u$, which implies that CCALR = P_u/P_y. For example, when P_u/P_y = 0.25, the current highly ductile limit for h/t_w is 49.1 according to Equation 3. By substituting h/t_w = 49.1 and CCALR = 0.25 into Equation 4, we can get L/r_y = 94.0, which is a point (49.1, 94.0) on the sloping dotted line. The shaded region above the line therefore represents sections that do not satisfy highly ductile behavior, meaning that their CCALR is less than P_u/P_y. Clearly most of the considered cases are in the shaded area suggesting that current highly ductile limits cannot guarantee that deep columns with a constant axial load can always reach 4% drift without failure. One of the reasons for this discrepancy is that current provisions do not consider the adverse interactions that occur between L/r_y and h/t_w.

Fig. 15 shows the PDSR of each column subjected to different levels of an initial, constant axial load ratio P_g/P_y. It is clear that increasing h/t_w, L/r_y, or P_g/P_y all have a negative effect on PDSR. For example, when P_g/P_y = 0.4 as shown in Fig. 15(c), the PDSR of columns with L/r_y about 50 decreases significantly from 0.92 to 0.45 when h/t_w increases from 15.6 to 35.6. Similarly, for W24x335 columns with h/t_w = 15.6, increasing L/r_y from 48.3 to 79.9 reduces the PSDR from 0.92 to 0.69.

The simulation data suggests that the effect of P_g/P_y increases the higher it becomes, which means that the difference of PDSR between P_g/P_y = 0.3 and 0.4 is larger than the one between P_g/P_y = 0.2 and 0.3. For example, for the W24x207 column with h/t_w = 24.8 and L/r_y = 80, the PDSR decreases from 0.77 to 0.7 when P_g/P_y increases from 0.2 to 0.3, and quickly decreases to 0.49 when P_g/P_y increases to 0.4.

Axial Shortening

It is well documented (Elkady and Lignos 2015, Uang et al. 2015, Elkady and Lignos 2016, and Fogarty et al. 2017) that axially loaded deep columns subjected to cyclic lateral drift shorten due to flange and web local buckling. Fig. 16 shows the evolution of axial shortening for a range of W24 prototype columns with P_g/P_y = 0.2 and 0.4. The amount of axial shortening in Fig. 16 is computed when the columns first reach drift levels between 0% and 4% and then normalized by column length (3.96 m). Also plotted are recent experimental results from Elkady and Lignos (2016). Fig. 16 shows data from specimens C5 (W24x146) and C8 (W24x84), both of which are subjected to a constant axial load of 0.2P_y combined with a collapse-consistent lateral loading protocol as defined by Elkady and Lignos (2016). The axial shortening plotted corresponds to that achieved when the columns first reach 1%, 2%, 3% and 4% drift levels. Clearly, the experimental data is consistent with the computational one, providing yet more confidence in the validity of computational scheme.

Two trends are clear from Fig. 16: 1) the amount of axial shortening depends greatly on the level of axial load (the curves for P_g/P_y = 0.4 are higher than those for P_g/P_y = 0.2); 2) the rate of growth of shortening is faster at the higher axial load level. Another key observation from Fig. 16 is that the amount of shortening is small at 1% drift, which is commonly associated with the immediate occupancy performance objective (ASCE 2006). At that level, the axial shortening is 0.1% and 0.3% when P_g/P_y = 0.2 and 0.4, respectively. Even at 2% drift, at which nonstructural damage is anticipated to occur, the amount of axial shortening is still small (substantially than 1% shortening).

The moment frame employed in this study has a span of 6.1 m and first-story clear height of 3.96 m. A relative axial shortening of 0.3% translates into a relative vertical displacement of 1/500 of the span between the beam's ends. This relative vertical displacement is expected to cause minor non-structural damage per serviceability requirements in AISC (2016c), if any, especially for performance levels associated with immediate occupancy. At 4% drift, nominally associated with the collapse prevention performance level, axial shortening is substantial, reaching more than 2% in the sections selected for study. However, these columns are still capable of supporting their axial load in accord with the objective of collapse prevention.

PROPOSED DESIGN GUIDELINES

As defined earlier, the CCALR can be interpreted as the maximum axial force that an interior column can support and still reach 4% drift. Assuming that the axial force on interior columns results from gravity loads and remains typically constant during an earthquake, Equation (4) can be rewritten as the following inequality:

$$\frac{P_g}{P_y} \le 0.72 - 0.0044\frac{h}{t_w} - 0.0027\frac{L}{r_y} \tag{6}$$

where P_g is the gravity-induced axial force. Rearranging Equation (6):

$$\frac{h}{t_w} \le 226(0.72 - \frac{P_g}{P_y}) - 0.62\frac{L}{r_y} \tag{7}$$

Based on the definition of CCALR, equation (7) suggests a way to get the highly ductile limit for h/t_w for interior columns, $\lambda_{hd,in}$. To frame equation (7) into a familiar format, it can be approximated and rearranged into the following form:

$$\lambda_{hd,in} = 9.86\sqrt{\frac{E}{R_y F_y}}(0.72 - \frac{P_g}{P_y}) - 0.62\frac{L}{r_y} \tag{8}$$

The PDSR can be interpreted as the maximum required strength that an exterior column must resist due to gravity loads and overturning moments. Based on this, Equation (5) can be rewritten to derive the relationship between the required axial strength of an exterior column, its section properties and the initial axial force level, i.e. the gravity-induced axial force, P_g:

$$\frac{P_r}{P_y} \le 1.71 - 0.011\frac{h}{t_w} - 0.0055\frac{L}{r_y} - \frac{P_g}{P_y} \tag{9}$$

where P_r is the required axial compressive strength as determined using the overstrength seismic load combined with the gravity-induced axial force. Rearranging Equation (9):

$$\frac{h}{t_w} \le 95(1.71 - \frac{P_g}{P_y} - \frac{P_r}{P_y}) - 0.53\frac{L}{r_y} \tag{10}$$

which indicates the highly ductile limit for h/t_w for exterior deep columns, $\lambda_{hd,ex}$, and can be approximated and reformatted into:

$$\lambda_{hd,ex} = 4.13\sqrt{\frac{E}{R_y F_y}}(1.71 - \frac{P_g}{P_y} - \frac{P_r}{P_y}) - 0.53\frac{L}{r_y} \tag{11}$$

To assess the effectiveness of the proposed equations, two W24, W27, and W30 columns each (not considered in the calibration process) are analyzed using the finite element (FE) models developed earlier and their capacities are compared to the values obtained from the proposed predictive functions (Equations 4 and 5 based on which Equations 8 and 11 are proposed). The properties of these columns and their performance parameters as well as predicted strength values are listed in Table 2. As can be seen, the predictive functions give comparable CCALR and PDSR values to the FE results for all columns with differences within 12% showing that the proposed guidelines are reasonably accurate and broad.

CONCLUSIONS

The collapse response of individual deep columns is investigated using a validated computational modeling scheme. To ensure that the loading and boundary conditions applied to the individual column models are realistic, collapse analyses of a four-story SMF are first performed to develop representative loading protocols and boundary conditions for first-story columns in earthquake-induced collapse scenarios, including both sidesway and vertical progressive collapse situations. The effects of the developed loading and boundary conditions on column behavior as compared to those used by others are highlighted and discussed. Using the developed loading protocols and boundary conditions, the collapse behavior of a variety of deep columns that cover a wide range of global and local slenderness ratios is studied. The key variables that influence response are identified and quantified through a regression analysis. Based on the limits of the parameters studied, the following conclusions can be drawn:

- The first-story drift histories in the system analyses show a cyclic ratcheting behavior, where the frame keeps leaning further and further until it collapses. While this behavior is seen in both sidesway and vertical progressive collapse modes, the overall characteristics of the histories are different. In vertical progressive collapse, the drift history does not increase as quickly as in sidesway collapse and collapse occurs at smaller drift levels, e.g. 2% to 6% versus about 10%.

- The performance of columns with a fix-pinned (FP) top end is substantially worse than columns with other boundary conditions. This behavior is because this particular type of boundary condition has essentially longer out-of-plane effective buckling length and is more prone to accumulation of local buckling at the top end, which reduces the end restraint and further increases the effective buckling length. On the other hands, columns with a spring-fixed (SF) top end generally have the highest drift capacities because they suffer less local buckling at their top ends and hence do not see as rapid a degradation in the top restraint as in their FP counterparts.
- Columns under the symmetric cyclic loading protocol (SC) show much worse drift capacity than other loading protocols. The lateral strength of the SC-loaded column at 4% drift was seen to be as low as 40% of that for columns with other loading protocols. The SC protocol tends to cause substantial local buckling at both sides of the column end, significantly degrading the ends restraints and thereby reducing the buckling strength of the columns and hence their axial loading capacity.
- Under the selected loading and boundary conditions, the web slenderness ratio, h/t_w, global slenderness ratio, L/r_y, and initial constant axial load ratio, P_g/P_y all have a significant effect on collapse capacity of deep columns. Generally, the effect of h/t_w on post-drift strength is larger than L/r_y, and the effect of P_g/P_y increases the higher it becomes. The simulation results also clearly show that current highly ductile limits specified in AISC design guidelines cannot guarantee that deep columns can reach 4% drift without failure.
- Both simulation results and recent experimental results show that the amount of column shortening is minimal for small drifts associated with the immediate

occupancy performance level. While column shortening increases significantly at 4% drift and may cause some nonstructural damage, columns still have capacity to support the required axial load in accord with the collapse prevention performance level. Column shortening is therefore a serviceability issue rather than safety concern.

Based on the comprehensive understanding developed in this work, design-oriented expressions are proposed to compute the compressive capacity of deep columns that are highly ductile in the AISC (2016a) sense. The proposed expressions are put into a familiar format to facilitate their adoption into future design provisions. These guidelines were developed using a limited set of sections and parameters. Therefore, additional work is needed to ensure that they are more generally applicable and incorporate appropriate resistance factors.

ACKNOWLEDGEMENTS

This work was supported by the University of Michigan and US NSF grant numbers CMMI-1344372 and ACI-1638186. Any opinions, findings, conclusions, and recommendations expressed in this paper are those of the authors and do not necessarily reflect the views of the sponsor.

REFERENCES

AISC. (2016a). *Seismic Provisions for Structural Steel Buildings*, *ANSI/AISC 341-16*, American Institute for Steel Construction, Chicago, IL

AISC. (2016b). *Prequalified Connections for Special and Intermediate Steel Moment Frames for Seismic Applications*, *ANSI/AISC 358-16* American Institute for Steel Construction, Chicago, IL

AISC. (2016c). *Specification for Structural Steel Buildings*, *ANSI/AISC 360-16*, American Institute for Steel Construction, Chicago, IL

Arasaratnam, P., Sivakumaran, K. S., and Tait, M. J. (2011). “True stress-true strain models for structural steel elements.” *ISRN Civil Eng.*, 2011, 1–11

ASCE. (2006). *Seismic Rehabilitation of Existing Buildings. ASCE/SEI 41-06*, American Society of Civil Engineers, Reston, VA

ASCE. (2010). *Minimum Design Loads for Buildings and Other Structures*. *ASCE/SEI 7-10*, American Society of Civil Engineers, Reston, VA

Elkady, A., and Lignos, D.G. (2015). “Analytical investigation of the cyclic behavior and plastic hinge formation in deep wide-flange steel beam-columns.” *Bull Earthquake Eng.*, 13, 1097-1118.

Elkady, A., and Lignos, D.G. (2016). “Dynamic Stability of Deep and Slender Wide-Flange *Steel* Columns – Full Scale Experiments.” *Proc. of Annual Stability Conference*, SSRC, Chicago, IL.

Engelmann, B. E., Whirley, R. G., and Goudreau, G. L. (1989). “A simple shell element formulation for large-scale elastoplastic analysis.” *Analytical and computational models of shells*, Noor AK, Belytschko T, and Simo JC, ASME, New York, NY

FEMA. (2009). “Quantification of building seismic performance factors.” *Report No. FEMA-P695*, Federal Emergency Management Agency, Washington, D.C.

Fogarty, J., and El-Tawil, S. (2015). “Collapse resistance of steel columns under combined axial and lateral loading.” *J. Struct. Eng.*, 10.1061/(ASCE)ST.1943-541X.0001350, 04015091.

Fogarty, J., Wu, T.-Y., and El-Tawil, S. (2017). “Collapse Response and Design of Deep Steel Columns Subjected to Lateral Displacement.” *J. Struct. Eng.*, accepted.

Huang, Y., and Mahin, S. A. (2010). “Simulating the inelastic seismic behavior of steel braced frames including the effects of low-cycle fatigue.” *Rep. No. PEER 2010/104*, Pacific Earthquake Engineering Research Center, Univ. of California at Berkeley, CA

HyperMesh Version 12.0 (2013). Altair Engineering Inc., Troy, MI

LS-DYNA (2013). Livermore Software Technology Corp., Livermore, CA

NIST. (2010). “Evaluation of the FEMA P695 methodology for quantification of building seismic performance factors.” *NIST GCR 10-917-8,* NEHRP consultants Joint Venture.

NIST. (2011). “Research plan for the study of seismic behavior and design of deep, slender wide flange structural steel beam-column members.” *NIST GCR 11–917-13*, NEHRP consultants Joint Venture.

Uang, C.M., Ozkula, G., and Harris, J. (2015). “Observations from cyclic tests on deep, slender wide-flange structural steel beam-column members.” *Proc. of Annual Stability Conference*, SSRC, Chicago, IL.

Wu, T.-Y, El-Tawil, S., and McCormick, J. (2017). “Behavior of steel moment frames with deep column sections under seismic loading.” *16th. World Conference on Earthquake Engineering*, Santiago, Chile

Table 1. Global and local slenderness ratios of prototype columns in parametric study of section properties

Section (in. x lb/ft)	$b_f/2t_f$	h/t_w	L/r_y	CCALR	PDSR $P_g/P_y = 0.2$	PDSR $P_g/P_y = 0.3$	PDSR $P_g/P_y = 0.4$
W24x55	6.94	54.6	116.4	0.20	-[a]	-[a]	-[a]
W24x76	6.61	49.0	81.3	0.30	0.57	-[a]	-[a]
W24x84	5.86	45.9	80.0	0.30	0.63	0.47	-[a]
W24x103	4.59	39.2	78.4	0.30	0.68	0.53	-[a]
W24x131	6.70	35.6	52.5	0.40	0.84	0.67	0.50
W24x162	5.31	30.6	51.1	0.45	0.93	0.83	0.68
W24x207	4.14	24.8	50.6	0.45	0.97	0.90	0.78
W24x335	2.73	15.6	48.3	0.55	1.00	1.00	0.92
W27x102	6.03	47.1	78.1	0.25	0.54	0.30	-[a]
W27x114	5.41	42.5	77.1	0.30	0.62	0.36	-[a]
W27x161	6.49	36.1	52.0	0.35	0.79	0.66	0.45
W27x217	4.71	28.7	50.6	0.45	0.90	0.88	0.66
W27x368	2.96	17.3	48.3	0.50	1.00	0.98	0.88
W30x108	6.89	49.6	83.7	0.20	0.47	-[a]	-[a]
W30x148	4.44	41.6	78.9	0.30	0.62	0.35	-[a]
W30x235	5.02	32.2	51.3	0.45	0.83	0.82	0.59
W30x357	3.45	21.6	49.6	0.45	1.00	0.94	0.85

[a]Not available because the column did not reach 4% drift under the applied P_g/P_y.

Table 2. Evaluation of linear predictive functions for CCALR and PDSR

Section (in. x lb/ft)	$b_f/2t_f$	h/t_w	L/r_y	CCALR		PDSR					
						P_g/P_y = 0.2		P_g/P_y = 0.3		P_g/P_y = 0.4	
				FE	Eq. (4)	FE	Eq. (5)	FE	Eq. (5)	FE	Eq. (5)
W24x94	5.18	41.9	93.9	0.25	0.28	0.53	0.54	-------[a]		-------[a]	
W24x146	5.92	33.2	67.8	0.40	0.38	0.82	0.78	0.76	0.68	-------[a]	
W27x94	6.70	49.5	107.5	0.20	0.20	0.43	0.39	-------[a]		-------[a]	
W27x307	3.46	20.6	73.9	0.40	0.42	0.86	0.88	0.81	0.78	0.65	0.68
W30x173	7.04	40.8	66.7	0.35	0.35	0.73	0.71	0.58	0.61	-------[a]	
W30x292	4.12	26.2	55.3	0.45	0.45	0.92	0.92	0.85	0.82	0.77	0.72

[a]Not computed because P_g/P_y is larger than CCALR in Eq. (4).

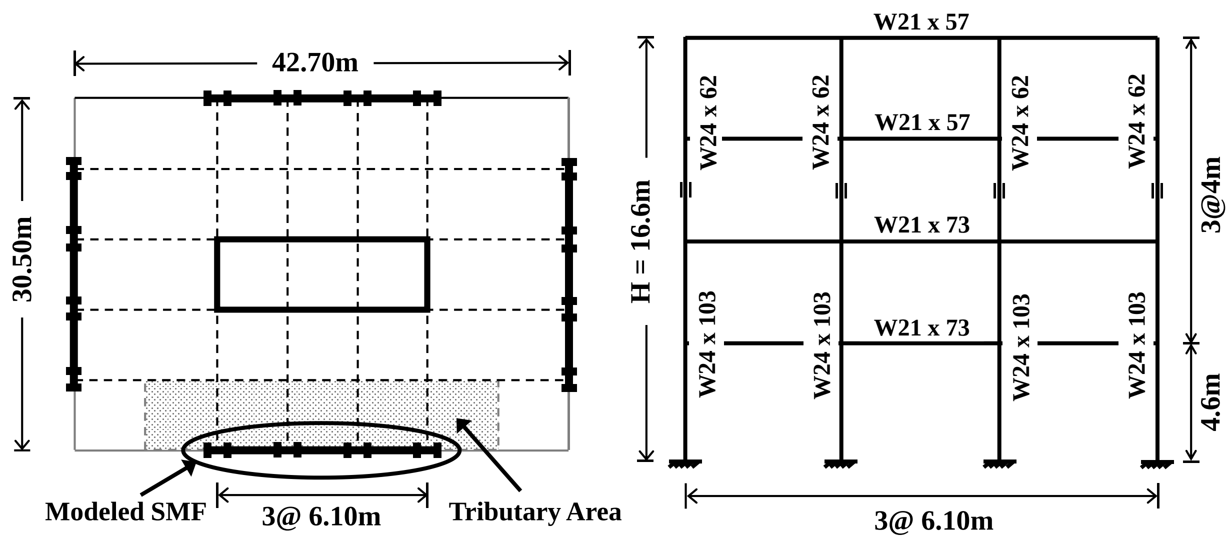

(a) (b)

Fig. 1. (a) Plan view of the four-story building; (b) elevation view of the modeled SMF.

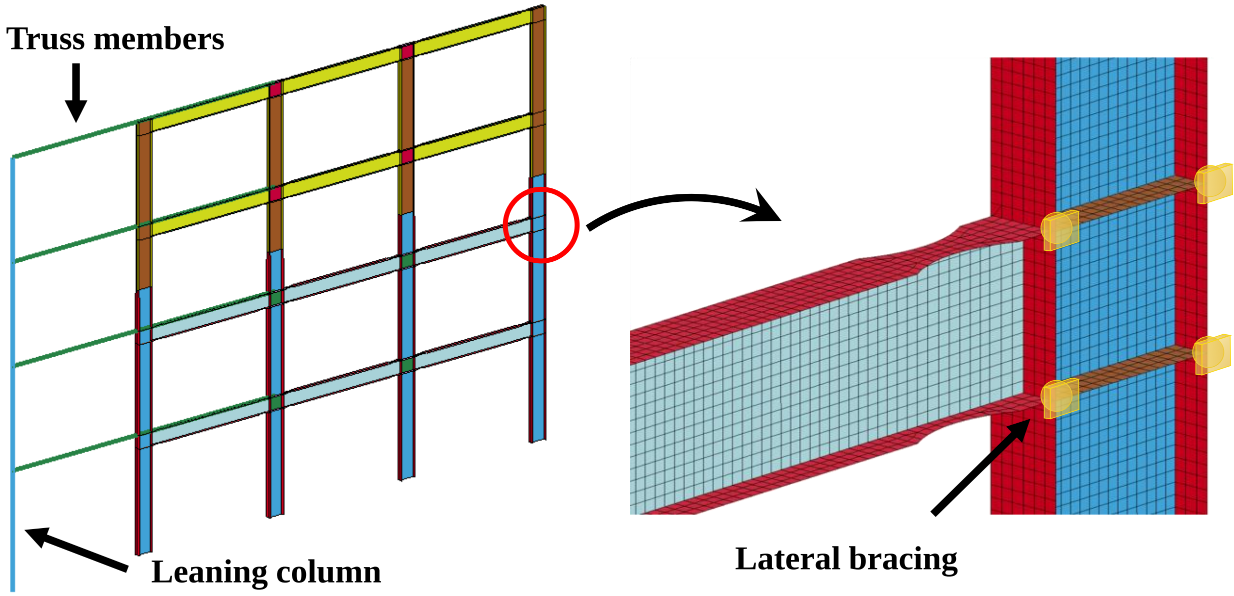

(a) (b)

Fig. 2. Finite element models of (a) four-story SMF; and (b) beam-to-column connections of four-story SMF

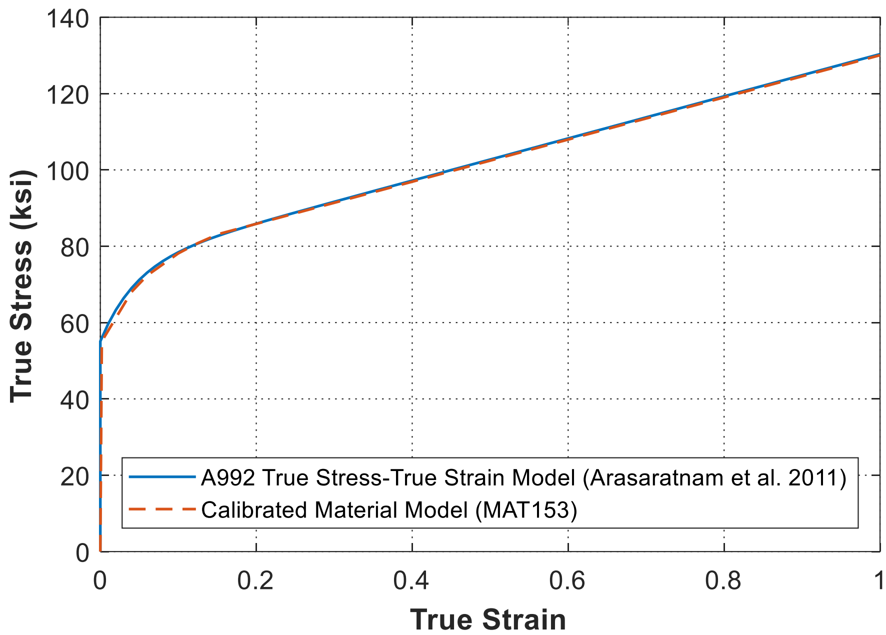

Fig. 3. Material model calibration with true stress-true strain model for A992 steel

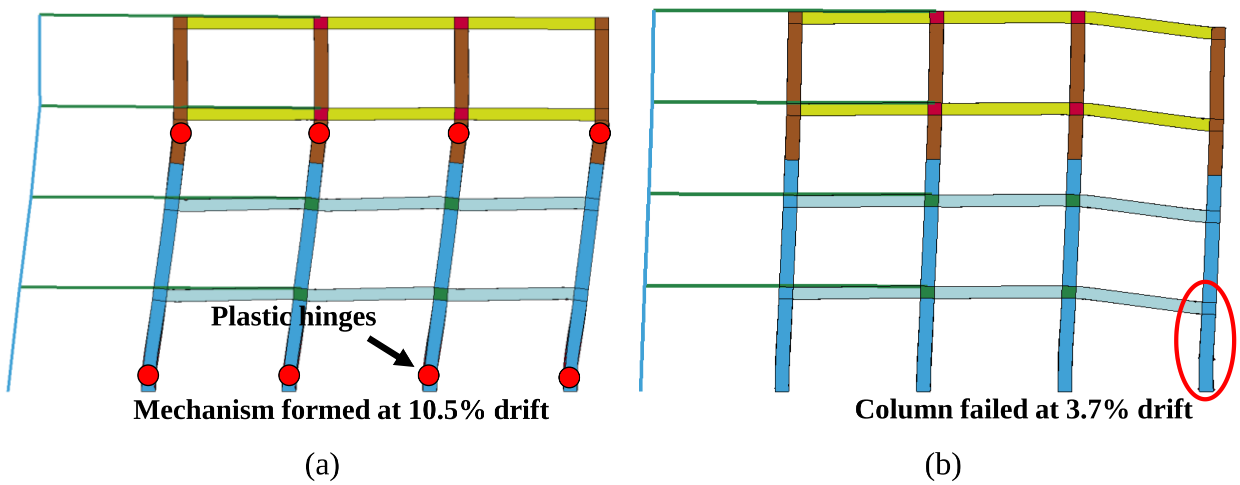

Fig. 4. (a) Sidesway collapse of TGL14 frame subjected to Northr/MUL009 record with S_a(1.67s, 5%)=1.61g; and (b) Vertical progressive collapse of TGL20 frame subjected to Northr/MUL009 record with S_a(1.67s, 5%)=1.19g

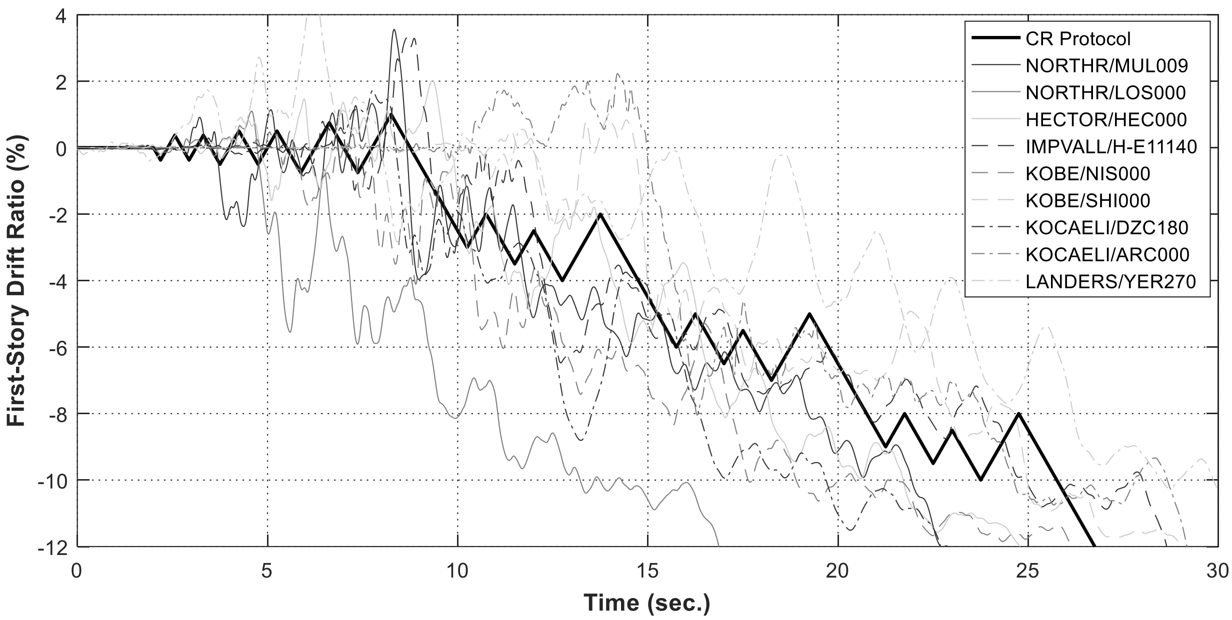

(a)

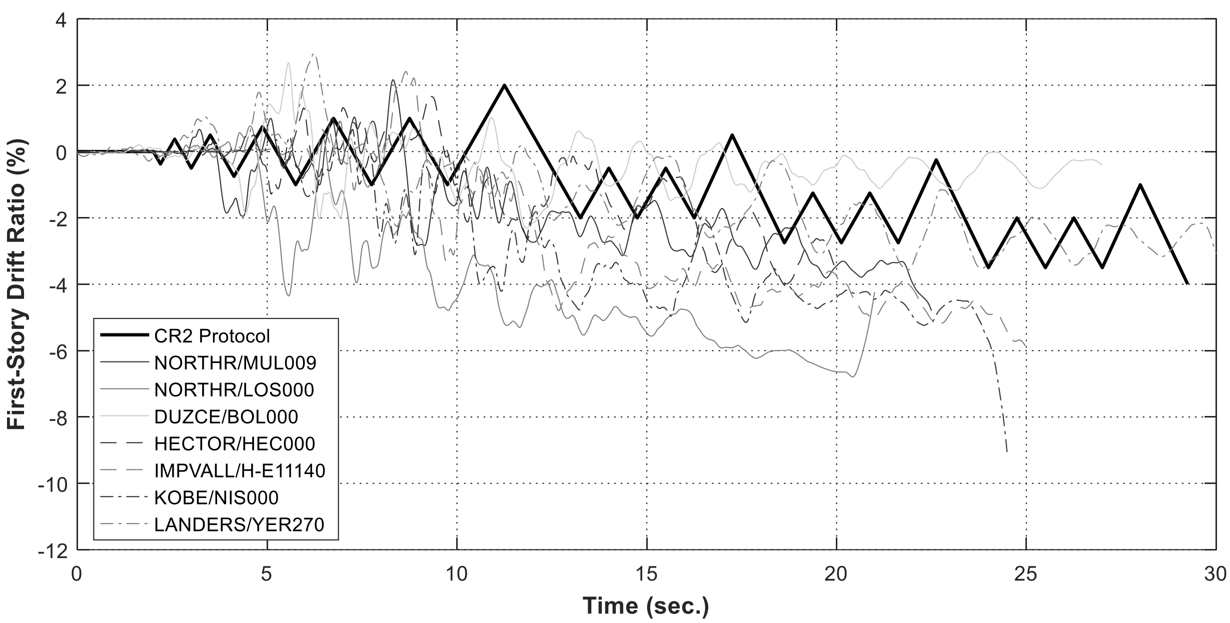

(b)

Fig. 5. (a) First-story drift history of TGL14 frame undergoing sidesway collapse; and (b) First-story drift history of TGL20 frame undergoing vertical progressive mechanism

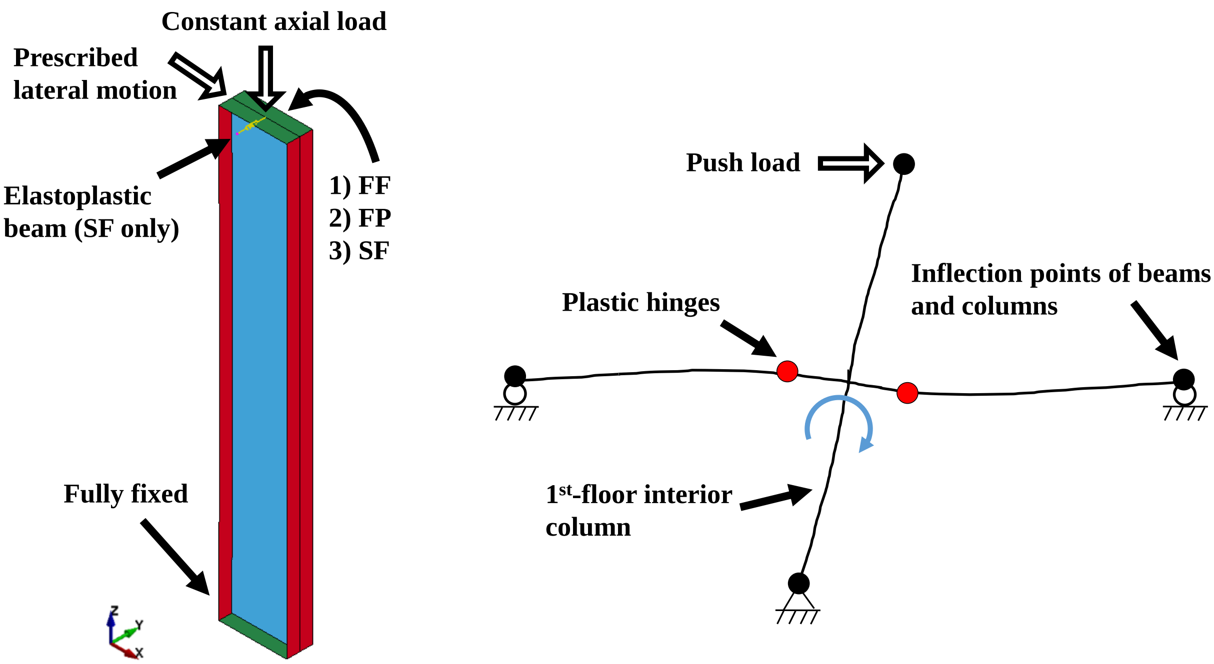

(a) (b)

Fig. 6. (a) Finite element models of individual deep columns; and (b) subassembly analysis for determining properties of elastoplastic spring

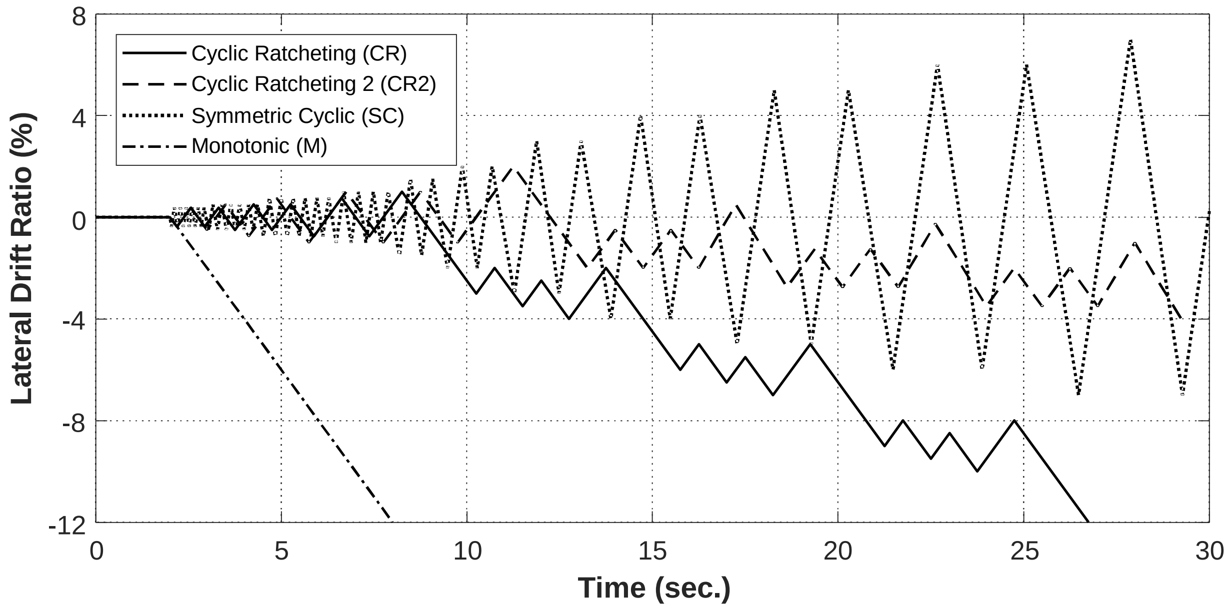

Fig. 7. Employed lateral drift loading protocols

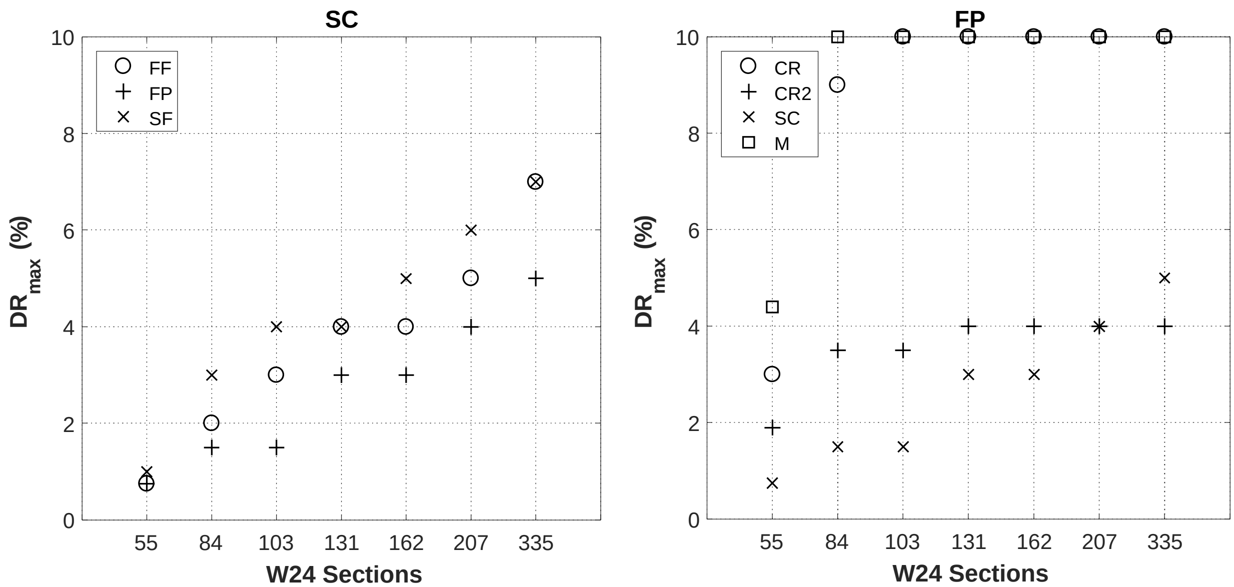

(a) (b)

Fig. 8. Maximum achieved drift ratios (DR_{max}) of columns with (a) different boundary conditions under SC protocol; and (b) different loading protocols under FP boundary condition

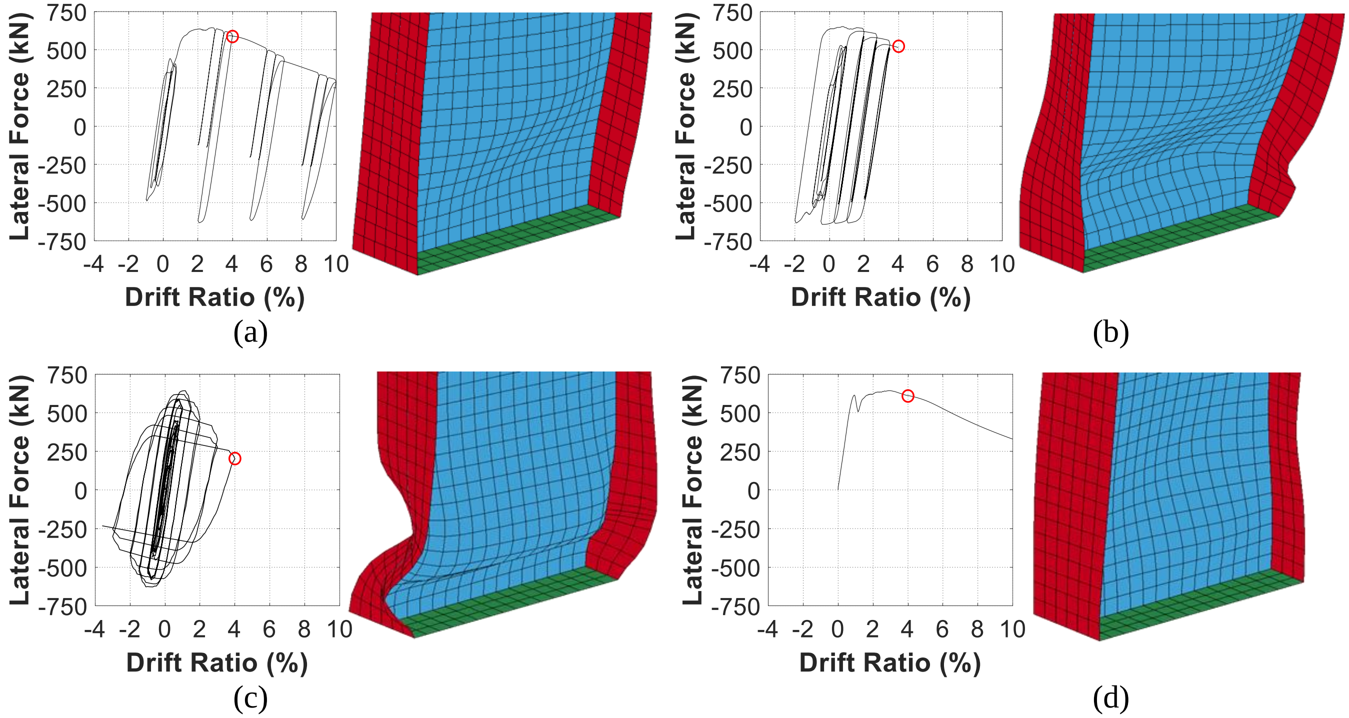

Fig. 9. Responses of W24x103 SF columns under different loading protocols and corresponding local buckling shapes at 4% drift marked by circles: (a) CR; (b) CR2; (c) SC; and (d) M. Displacement scale factor is 3.0.

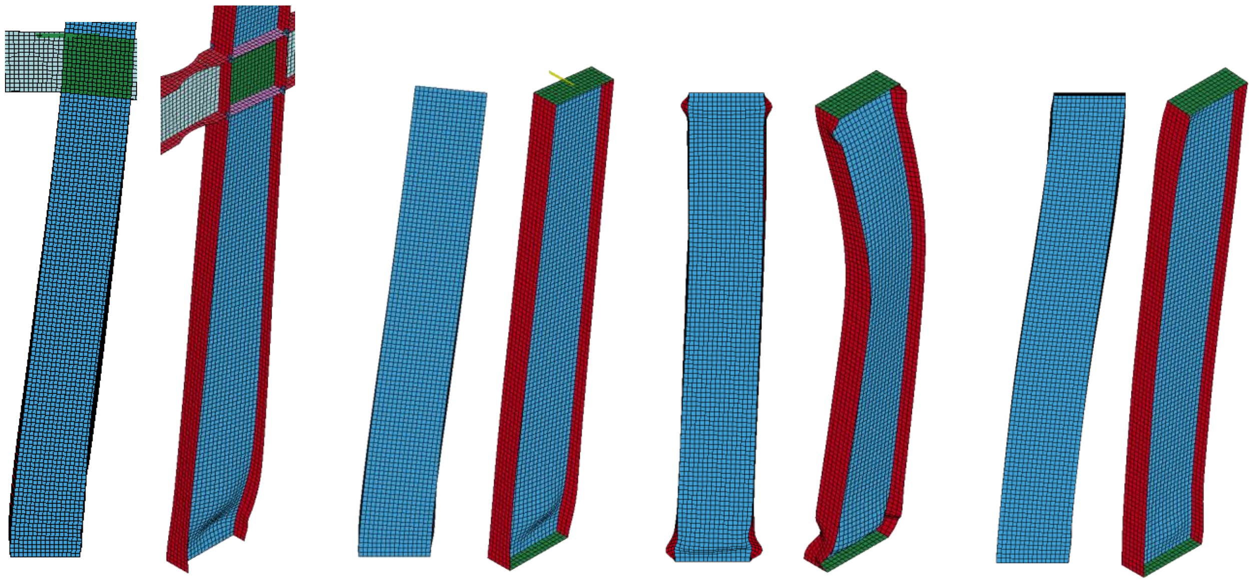

(a) (b) (c) (d)

Fig. 10. Comparison between deformed shape of columns at 4% drift: (a) interior column (W24x103) in TGL20 frame undergoing sidesway collapse; (b) W24x103-SF-CR; c) W24x103-FF-SC; and (d) W24x103-FP-M. Displacement scale factor is 3.0.

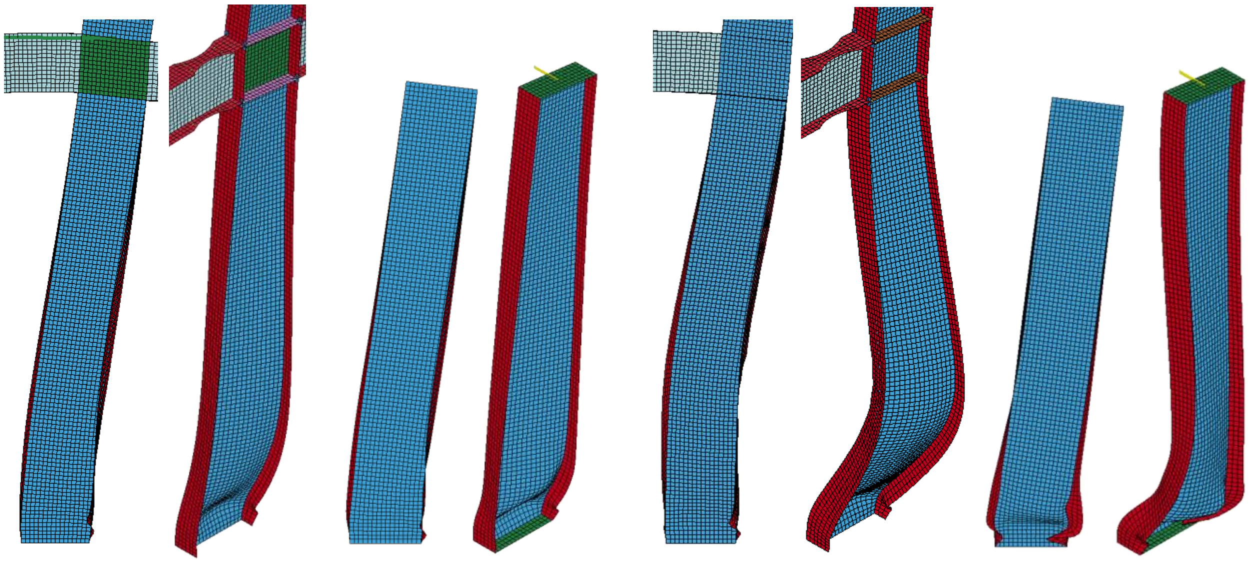

(a) (b) (c) (d)

Fig. 11. Comparison between deformed shape of columns at 4% drift (a) interior column (W24x103) in TGL20 frame undergoing vertical progressive collapse; (b) W24x103-SF-CR2; (c) exterior column (W24x103) in TGL20 frame undergoing vertical progressive collapse; and (d) W24x103-SF-CR2 with halved spring properties. Displacement scale factor is 3.0.

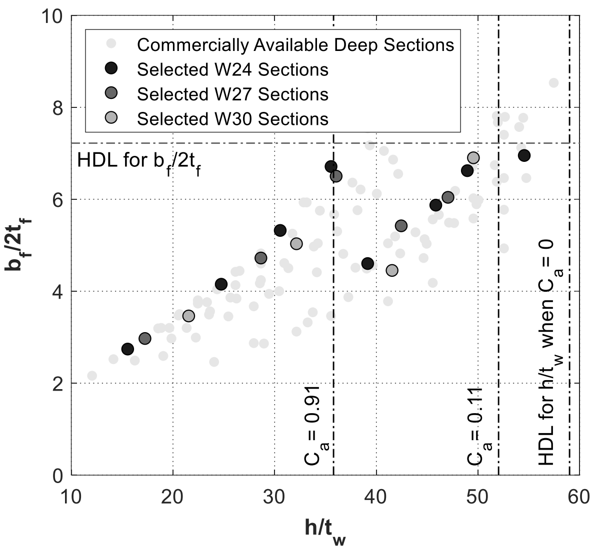

(a)

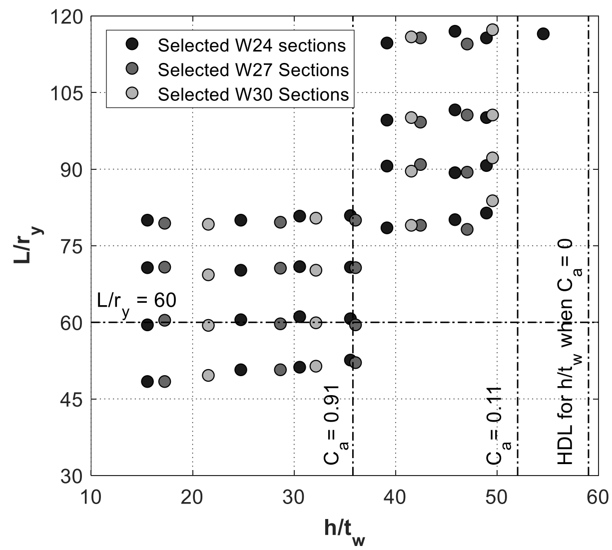

(b)

Fig. 12. Slenderness ratios of selected sections and commercially available deep, wide flange sections made of A992 steel: (a) h/t_w versus $b_f/2t_f$; and (b) h/t_w versus L/r_y

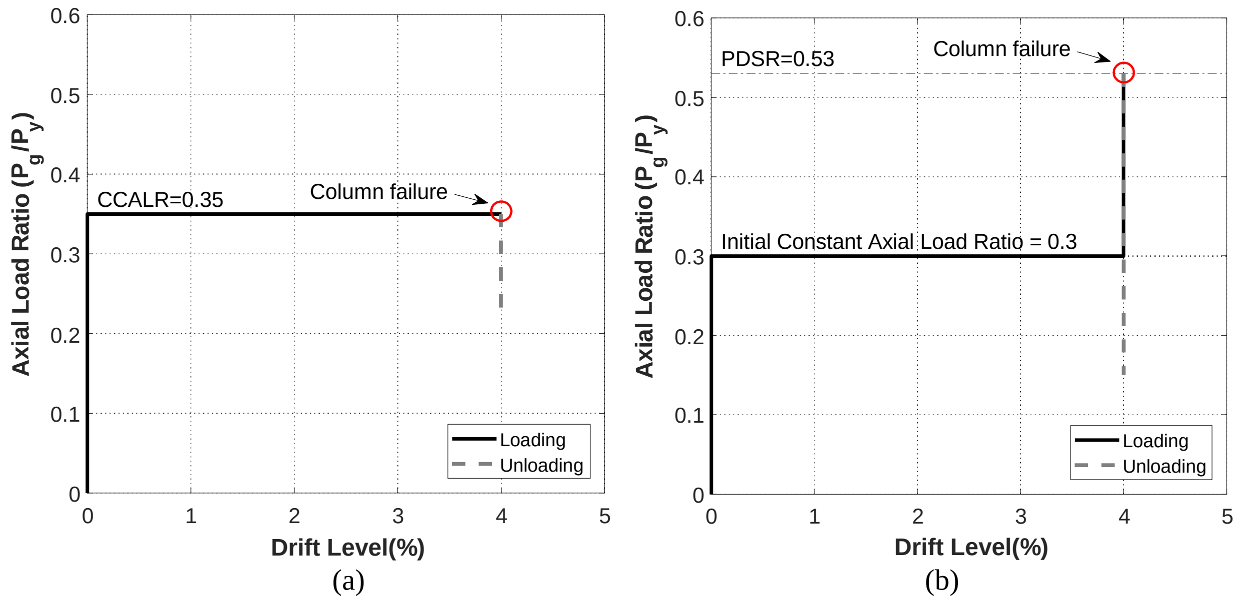

Fig. 13. Definition of performance parameters (a) CCALR and (b) PDSR

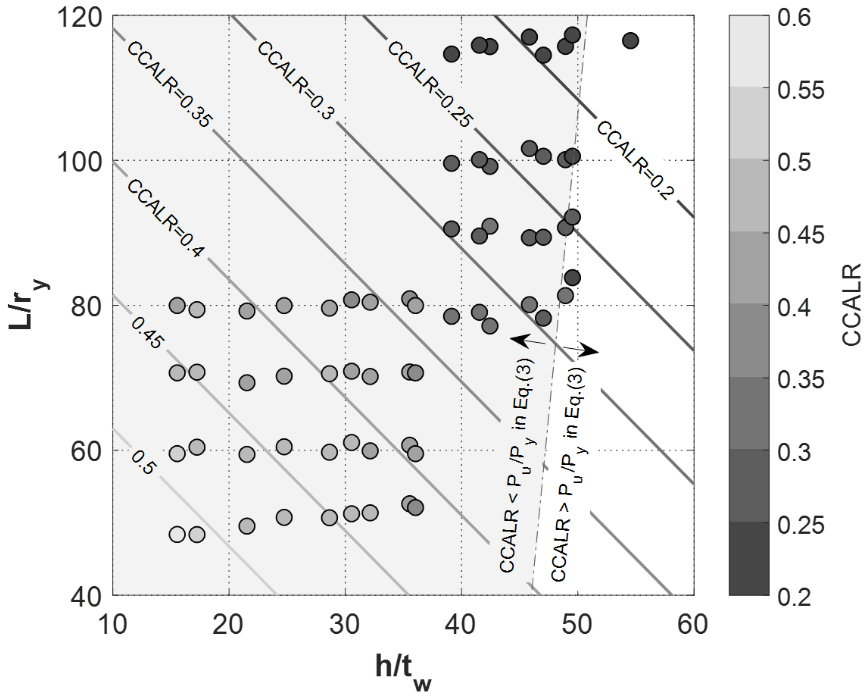

Fig. 14. Contour plot of predictive function for CCALR

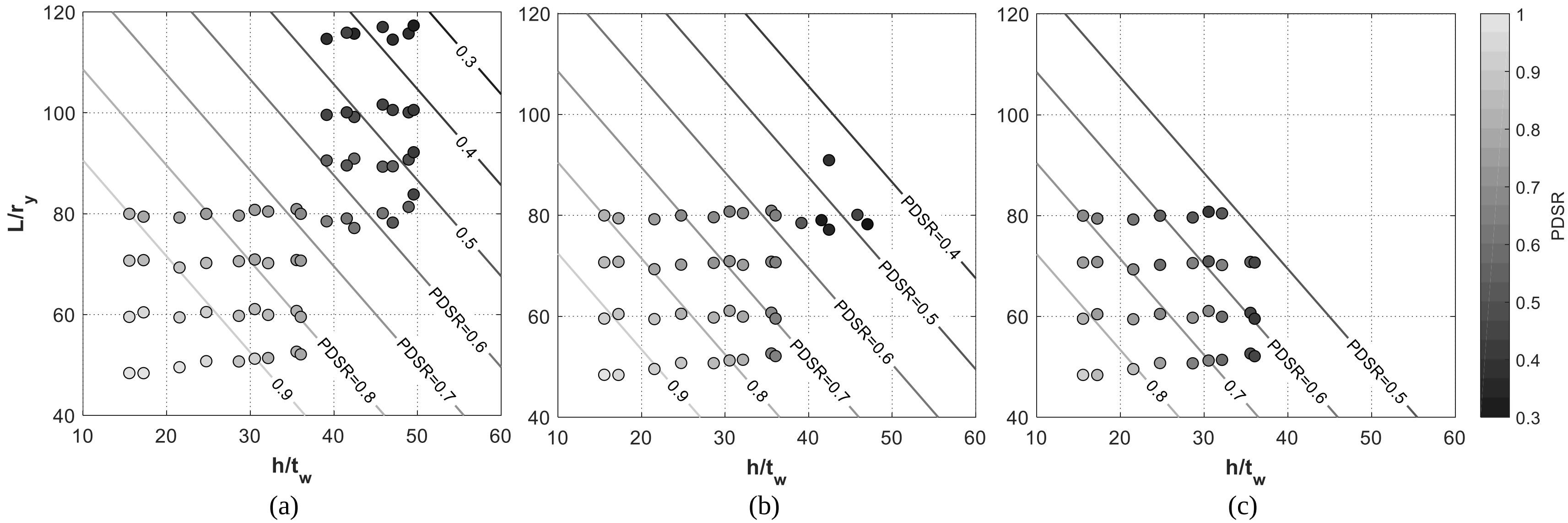

Fig. 15. Contour plot of predictive function for PDSR when initial constant axial load ratio P_g/P_y = (a) 0.2; (b) 0.3; and (c) 0.4

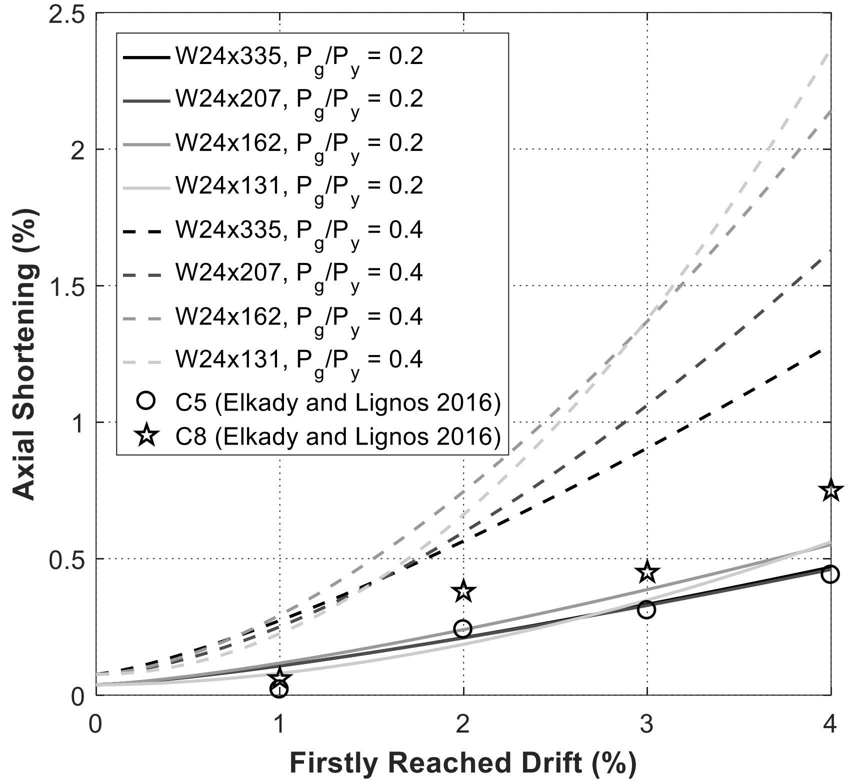

Fig. 16. Axial shortening evolution of W24 prototype columns subjected to an axial load of $0.2P_y$ or $0.4P_y$